nature nanotechnology

LETTERS

https://doi.org/10.1038/s41565-020-0770-x

Optical fibres with embedded two-dimensional materials for ultrahigh nonlinearity

Yonggang Zuo[1,2,9], Wentao Yu[2,9], Can Liu[2,9], Xu Cheng[2], Ruixi Qiao[3], Jing Liang[2], Xu Zhou[2], Jinhuan Wang[4], Muhong Wu[3], Yun Zhao[4], Peng Gao[3], Shiwei Wu[5], Zhipei Sun[6], Kaihui Liu[2,3]✉, Xuedong Bai[1]✉ and Zhongfan Liu[7,8]✉

Nonlinear optical fibres have been employed for a vast number of applications, including optical frequency conversion, ultrafast laser and optical communication[1–4]. In current manufacturing technologies, nonlinearity is realized by the injection of nonlinear materials into fibres[5–7] or the fabrication of microstructured fibres[8–10]. Both strategies, however, suffer from either low optical nonlinearity or poor design flexibility. Here, we report the direct growth of MoS_2, a highly nonlinear two-dimensional material[11], onto the internal walls of a SiO_2 optical fibre. This growth is realized via a two-step chemical vapour deposition method, where a solid precursor is pre-deposited to guarantee a homogeneous feedstock before achieving uniform two-dimensional material growth along the entire fibre walls. By using the as-fabricated 25-cm-long fibre, both second- and third-harmonic generation could be enhanced by ~300 times compared with monolayer MoS_2/silica. Propagation losses remain at ~0.1 dB cm^{-1} for a wide frequency range. In addition, we demonstrate an all-fibre mode-locked laser (~6 mW output, ~500 fs pulse width and ~41 MHz repetition rate) by integrating the two-dimensional-material-embedded optical fibre as a saturable absorber. Initial tests show that our fabrication strategy is amenable to other transition metal dichalcogenides, making these embedded fibres versatile for several all-fibre nonlinear optics and optoelectronics applications.

The superiority of two-dimensional (2D) materials used in nonlinear optical fibres is that (1) the atomically thin layer does not destroy the high-quality waveguide modes in the fibres and (2) the enhanced light–2D material interaction within the fibres can induce ultrahigh nonlinear optical responses[12–14]. Previously, 2D materials were mainly attached to optical fibres by transfer techniques, unfortunately suffering from distortions in propagation capacity, shorter light–material interaction length and difficulty in batch manufacturing[15–17]. Owing to the great progress made in 2D material growth, it is now possible to directly fabricate graphene optical fibres, wherein the feedstock is in the gas phase and therefore relatively easy to diffuse into narrow holes for homogeneous growth[18]. However, in transition metal dichalcogenide (TMD)-embedded optical fibre growth, the typical feedstocks are solid precursors and thus very difficult to transfer into the fibre holes effectively and homogeneously[19–22].

To alleviate this dilemma, the key design aspect of our method lies in the pre-deposition step, as shown in Fig. 1a. Mo sources were filled into the fibre holes by the capillarity of the Na_2MoO_4 aqueous solution. After that, the fibre was loaded into a chemical vapour deposition (CVD) furnace to bake for 30 min at a low temperature of 110 °C for dewetting, and the Na_2MoO_4 precursors gather into clusters and are randomly coated onto the inner fibre walls, serving as a storage site for the Mo sources (Fig. 1a, middle). Subsequently, at a high growth temperature of ~820 °C, Na_2MoO_4 clusters on the hole walls transform into liquid droplets and continuously release Mo precursors under vapourization in the confined narrow space of the fibre holes[23]. Sulfur vapour was carried by argon gas from the upstream direction via a low-pressure pump and then uniformly mixed with Na_2MoO_4 vapour for the subsequent homogeneous MoS_2 growth (Fig. 1a, right, and Supplementary Note 1).

In our two-step growth method, the MoS_2 coverage and thickness can be facilely tuned by the concentration (c) of Na_2MoO_4 in the solution. When we increased the solute concentration from 1 to 4 to 8 mg ml^{-1}, the MoS_2 gradually enlarged from 40 μm triangles (Fig. 1b), 250 μm triangles (Fig. 1c) and a continuous film (Fig. 1d), respectively. A further increase in the Na_2MoO_4 concentration led to the growth of few-layered MoS_2 (Supplementary Figs. 1 and 2). Under our optimized conditions, we could readily realize homogeneous MoS_2 growth onto the hole walls of a long optical fibre up to 25 cm (Supplementary Fig. 3). Further, we also carried out controlled experiments, in which instead of the pre-deposition of Mo precursor onto the walls of the fibre holes, MoO_3 was directly sent from outside the fibres (as performed in prevailing growth methods[24]); we found that only a few distributed MoS_2 islands could be grown using this strategy (Supplementary Fig. 4). Thus, the pre-deposition of the Mo source in the fibre holes is the key step for the successful growth of large and uniform MoS_2 films onto the fibres.

A high-quality MoS_2 film grown in the confined spaces of the fibre holes is comparable to that grown on flat substrates in free space, which can be fully confirmed by the photoluminescence (PL) mapping (Supplementary Fig. 5) data of the individual triangular domain. These triangles are single-crystal domains, as proven by the parallel polarization second-harmonic-generated (SHG) patterns at different positions of the single domain (Fig. 1f). Further, we etched away the fused silica fibre and transferred the MoS_2 film

[1]Beijing National Laboratory for Condensed Matter Physics, Institute of Physics, Chinese Academy of Sciences, Beijing, China. [2]State Key Laboratory for Mesoscopic Physics, Frontiers Science Center for Nano-optoelectronics, School of Physics, Peking University, Beijing, China. [3]International Centre for Quantum Materials, Peking University, Beijing, China. [4]School of Chemistry and Chemical Engineering, Beijing Institute of Technology, Beijing, China. [5]State Key Laboratory of Surface Physics, Department of Physics, Fudan University, Shanghai, China. [6]Department of Electronics and Nanoengineering and QTF Centre of Excellence, Aalto University, Aalto, Finland. [7]Center for Nanochemistry, College of Chemistry and Molecular Engineering, Peking University, Beijing, China. [8]Beijing Graphene Institute (BGI), Beijing, China. [9]These authors contributed equally: Yonggang Zuo, Wentao Yu, Can Liu. ✉e-mail: khliu@pku.edu.cn; xdbai@iphy.ac.cn; zfliu@pku.edu.cn

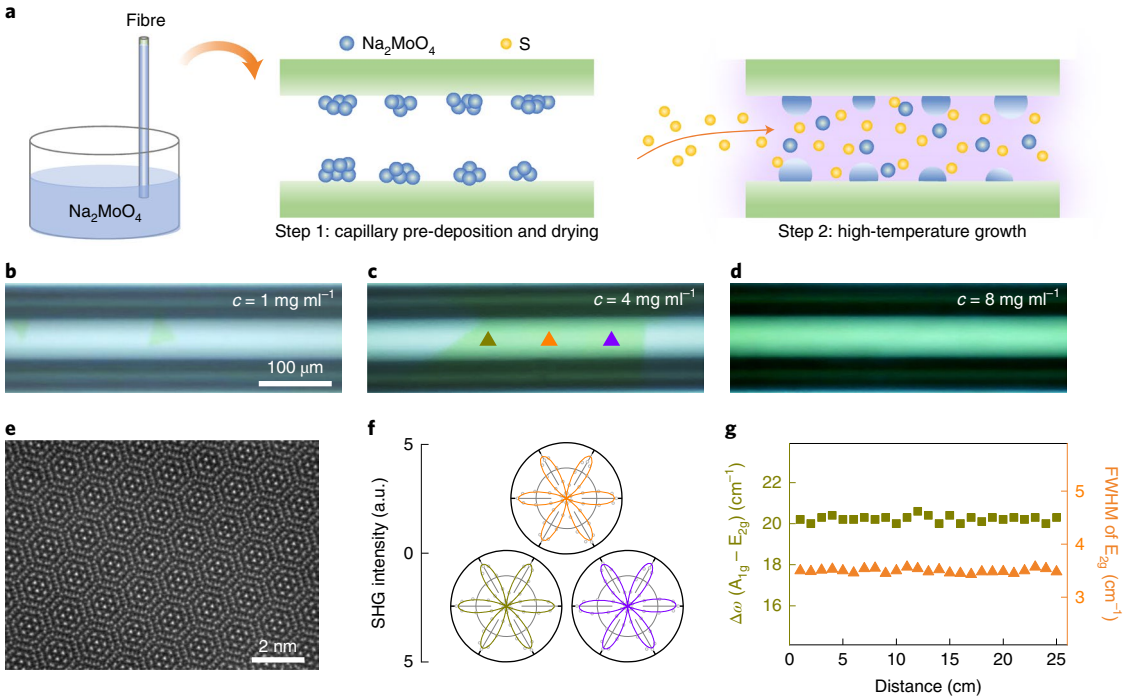

Fig. 1 | Two-step growth of a high-quality, uniform, monolayer MoS_2-embedded optical fibre. a, Schematic of the designed two-step growth method, consisting of the pre-deposition of Na_2MoO_4 onto the walls of the fibre holes by capillary filling and low-temperature drying followed by high-temperature growth. **b**–**d**, Dependence of MoS_2 coverage on the Na_2MoO_4 aqueous solution concentrations of 1 mg ml^{-1} (**b**), 4 mg ml^{-1} (**c**) and 8 mg ml^{-1} (**d**), respectively. **e**, STEM image of collapsed tube-like MoS_2 transferred onto a hollow grid, showing the high crystallinity of the as-grown MoS_2 without detectable defects. **f**, Parallelly polarized SHG patterns at the different positions labelled in **c**, revealing that the whole MoS_2 domain is a large single crystal. **g**, Statistical $\Delta\omega$ ($A_{1g} - E_{2g}$) (the frequency difference of Raman shift (ω) between A_{1g} peak and E_{2g} peak; left *y* axis) and FWHM values of the E_{2g} peak (right *y* axis) plotted as a function of the numbered sites on the MoS_2-embedded fibre along the whole length of 25 cm. The slight variations prove that the MoS_2 film is uniformly grown onto the fibre.

onto a hollow grid for scanning transmission electron microscopy (STEM) characterization with atomic resolution. When the tube-like MoS_2 monolayer collapsed (Supplementary Fig. 6), a clear moiré pattern of the MoS_2 bilayers became evident without observable defect sites (Fig. 1e), reconfirming the formation of high-quality MoS_2 domains. Furthermore, marginal variations in the frequency difference between A_{1g} and E_{2g} as well as the narrow distribution of the full-width at half-maximum (FWHM) values of the E_{2g} peak in the Raman spectra along the entire 25-cm-long fibre indicated that the as-grown monolayer MoS_2 film was highly uniform[25,26] (Fig. 1g).

Our growth method for the MoS_2-embedded optical fibre has been proven to be universal for different fibre structures and 2D materials. Two types of commonly used microstructured optical fibres, namely, hollow capillary fibres (HCFs) with different hole diameters (ranging from 5 to 15 to 50 μm (Fig. 2a and Supplementary Fig. 7)) and photonic crystal fibres (PCFs) with air or solid cores (Fig. 2b and Supplementary Fig. 8), were used to successfully grow uniform monolayer MoS_2 films (Fig. 2c,d). Since the diameter of the hole varies in different fibres, the amount of Mo precursor pre-deposited on the inner hole walls is accordingly adjusted via the solute concentration (that is, the smaller the diameter, the higher the Na_2MoO_4 concentration). This growth method has also been used to fabricate fibres with different TMDs simply by varying the feedstocks of the transition metals (for example, Na_2MoO_4 and Na_2WO_4) and chalcogen (for example, S and Se) species with adjusted growth temperatures (Methods). The Raman and PL spectra of these obtained homogeneous TMD-embedded fibres demonstrate the construction of optical fibres embedded with MoS_2, WS_2 and $MoSe_2$, as well as alloys such as MoS_xSe_{2-x} (Fig. 2e,f).

Due to their intact light propagation mode (Supplementary Fig. 9), strong light–matter interaction, various fibre structures and rich TMD species, 2D-material-embedded optical fibres afford ultra-high optical nonlinearity and plentiful function/design flexibility, which intuitively yields different potential applications in the wide scopes of nonlinear optics. Since the optical nonlinear susceptibility contains two parts, namely, the real part and imaginary part, the corresponding applications can be divided into two types: (1) nonlinear wavelength conversion (for example, harmonic generation and four-wave mixing frequency), which is the typical demonstration of the real part, and (2) nonlinear absorption (for example, saturable absorption and multiphoton absorption), which is the typical demonstration of the imaginary part[27]. By selecting proper fibre structures and 2D material species, applications related to the real and imaginary parts have been demonstrated using our TMD-embedded fibres.

We demonstrated that the nonlinear optical harmonic generation (SHG and third-harmonic generation (THG), as shown in Fig. 3a) from the TMD-embedded fibres was greatly enhanced compared with that from conventional optical fibres, wherein the SHG and THG were fairly weak and rarely observed before. With regard to practical nonlinear wavelength conversion, the real part of nonlinear susceptibility needs to be utilized, and simultaneously, it should be ensured that the excitation and emission of photons is within the bandgap of the materials. Since the MoS_2 monolayer has a direct bandgap of ~670 nm, we chose longer wavelengths (1,800 and 2,100 nm) to generate the SHG and THG (900 and 700 nm, respectively), where the incident and generated photon energies were both smaller than the bandgap to ensure low propagation loss at both the excited and emitted wavelengths (Supplementary

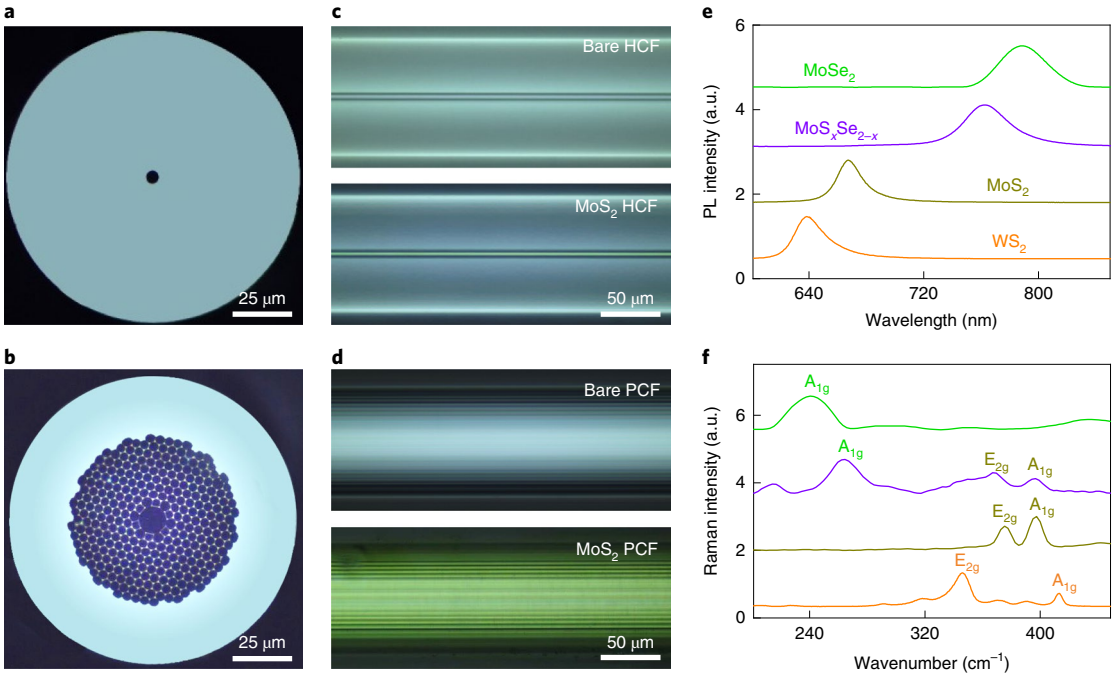

Fig. 2 | Two-dimensional-material-embedded optical fibres with diverse fibre structures and material species. a,**b**, Optical images of a HCF with a core diameter of ~5 μm (**a**) and a PCF with a hollow-core honeycomb structure (**b**). **c**,**d**, The corresponding side views of HCF (**c**) and PCF (**d**) shown in **a** and **b**, respectively. Higher contrast was observed after the growth of MoS_2 (bottom) compared with the bare ones (top). **e**,**f**, PL (**e**) and Raman (**f**) spectra of the fibres embedded with as-grown $MoSe_2$ (green), MoS_2 (dark yellow), WS_2 (orange) and MoS_xSe_{2-x} (violet). The PL and Raman spectra are shifted vertically for clarity.

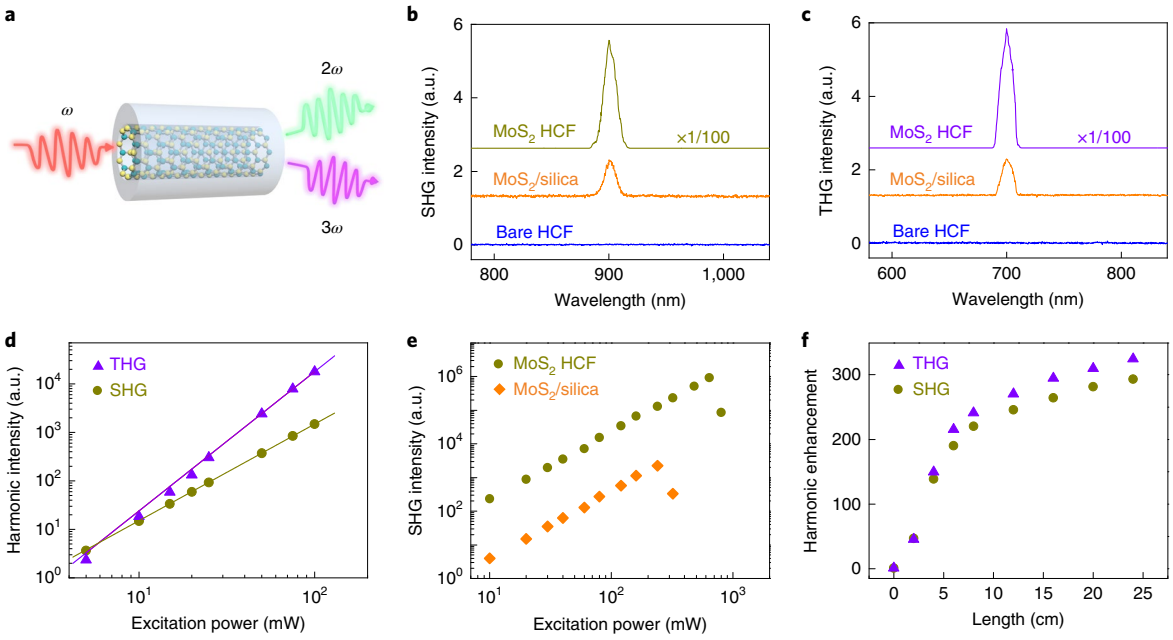

Fig. 3 | Greatly enhanced harmonic generation in MoS_2-embedded HCF. a, Schematics of SHG (2ω) and THG (3ω) in MoS_2-embedded HCF. **b**,**c**, SHG (**b**) and THG (**c**) spectra of MoS_2 HCF; MoS_2 on flat, fused silica substrate (MoS_2/silica); and bare HCF under 1,800 and 2,100 nm excitation, respectively. With the strong light–matter interaction in 25-cm-long MoS_2 HCF, both SHG and THG can be enhanced by ~300 times compared with monolayer MoS_2/silica. For comparison, no apparent SHG or THG signal can be observed in bare HCF. The SHG and THG spectra are shifted vertically for clarity. **d**, Excitation-power dependence of SHG and THG intensities for MoS_2 HCF, showing the as-expected quadratic and cubic laws. **e**, Measured SHG intensity of 12-cm-long MoS_2 HCF and MoS_2/silica as a function of the excitation power under 800 nm excitation. Benefiting from the larger mode area and evanescent light coupling, the damage threshold of MoS_2 HCF is about three times higher than that of MoS_2/silica. **f**, Fibre-length-dependent SHG and THG enhancements in MoS_2 HCF with respect to MoS_2/silica, showing a general monotonic increase and saturation behaviour with the fibre length.

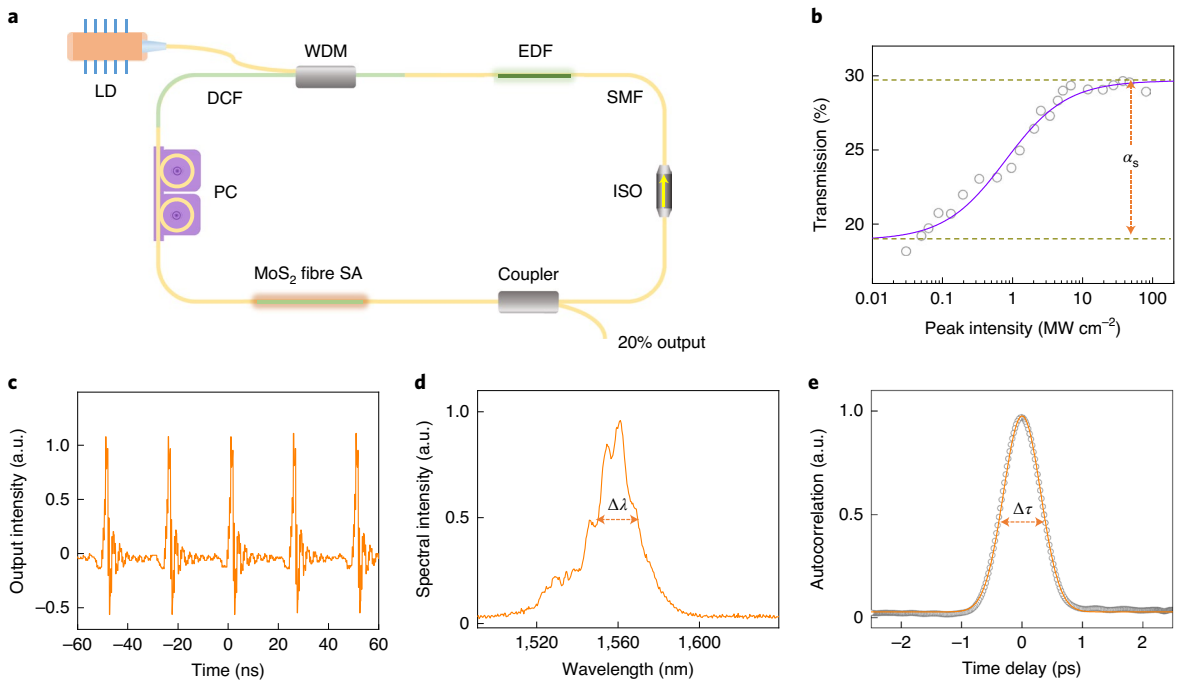

Fig. 4 | Ultrafast laser based on MoS_2-embedded PCF. a, Schematic of all-fibre mode-locked laser with MoS_2-embedded fibre as an SA. The optical components consist of a laser diode (LD), wavelength-division multiplexer (WDM), single-mode fibre (SMF), dispersion compensation fibre (DCF), erbium-doped fibre (EDF), isolator (ISO) and polarization controller (PC). **b**, Transmission measurement of the MoS_2 PCF for $\alpha_S \approx 10\%$ and saturation peak intensity of 0.8 MW cm^{-2}. The solid curve is fitted according to the experimental data (circles). **c**, Output pulse train with ~24 ns interval (~41 MHz repetition rate). **d**, Spectrum of the output laser with $\Delta\lambda \approx 19$ nm. **e**, Autocorrelation trace with FWHM ($\Delta\tau$) of ~720 fs fitted by a Gaussian function, corresponding to a pulse duration of ~500 fs.

Fig. 10). As per this design, we observed notably enhanced harmonic generation in monolayer MoS_2-based HCF with a length of up to ~25 cm, which is more than 300 times higher than that obtainable from monolayer MoS_2 on a flat, fused silica substrate (Fig. 3b,c). The square and cubic dependence of the emission intensity on the excitation power reveals that the observed signals are from the SHG and THG, respectively (Fig. 3d).

Another great advance of 2D-material-embedded optical fibres for nonlinear wavelength conversion is that they yield higher damage threshold power. Unlike the direct focusing of a laser on nonlinear materials in free space, light in the fibre can fill the waveguide core, typically resulting in a larger light-field area. Therefore, fibre optics can withstand much higher power before the nonlinear medium is damaged. Besides, the 2D materials on the fibre walls typically interact with the evanescent light, which is often weaker than light in the fibre core. For the HCF with a hollow core size of ~50 μm and wall thickness of ~40 μm, light can steadily propagate in the side wall (an annular fibre core) and output at the fibre end (Supplementary Fig. 11). The damage threshold power for the MoS_2-embedded fibre under the 800-nm-excited laser (with high power to reach the damage threshold) is about three times higher than that on a planar substrate with a focal spot of ~10 μm (Fig. 3e). Considering the enhancements in both light–matter interactions and damage threshold power, the output power of harmonic generation in monolayer MoS_2-embedded optical fibre is three orders of magnitude higher than that of planar 2D MoS_2; further, energy conversion can reach 10^{-4} to 10^{-3} (see Supplementary Note 2), which is already sufficiently high for some applications such as on-chip new wavelength generation and all-fibre optical parametric oscillator[28,29]. We also observed that the nonlinear enhancement shows a general monotonic increase and saturation behaviour with the fibre length (Fig. 3f). In principle, the SHG or THG signal should have quadratic dependence on the length[27], which is indeed the case for fibre lengths less than 5 cm. However, when the fibre becomes longer, the loss effect caused by the absorption tail of monolayer MoS_2 as well as the phase mismatch between the excitation and SHG/THG lights leads to the deviation from the quadratic increase and the saturation shows an upward trend.

Further, we utilized the MoS_2-embedded PCF as a saturable absorber (SA) in a fibre laser for ultrafast pulse generation, which is a typical example of imaginary-part-related applications. The laser structure is similar to the most commonly demonstrated fibre ring cavity, which contains a pump laser diode, an erbium-doped fibre (gain media) and an optical coupler as the output[15] (Fig. 4a). Here the main difference is that we replaced a conventional free-space SA film by the MoS_2-embedded fibre and therefore realized an all-fibre mode-locked laser. For exploiting the absorptive properties of 2D materials, we intentionally grew 6–8-layered MoS_2, which had a larger absorption tail at ~1,550 nm compared with that of the monolayer[30]. This 3-cm-long few-layered MoS_2 PCF with a hollow-core honeycomb structure shows a relatively low coupling loss of ~1 dB (Supplementary Fig. 12) and a nonlinear absorption modulation depth (α_S) of 10% with a saturation peak intensity of 0.8 MW cm^{-2} (Fig. 4b); these values are already comparable to those of conventional SA semiconductors[15] (for example, modulation depth of ~5% with a saturation peak intensity of ~2 MW cm^{-2} for AlAs/GaAs Bragg mirrors). Then, a stretched-pulse passively mode-locked fibre laser was built by dispersion management. The maximum output power of the pulsed laser is ~6 mW (under continuous-wave laser pump power of 600 mW and at room temperature) with ~41 MHz repetition frequency (Fig. 4c), ~19 nm spectral bandwidth ($\Delta\lambda$), 1,560 nm centre wavelength (Fig. 4d) and ~500 fs pulse duration (Fig. 4e and lasing reporting summary for more laser specifics). The subpicosecond pulse train shows a high signal-to-noise ratio

of ~52 dB (Supplementary Fig. 13). Considering the relatively broad spectral bandwidth (~19 nm), the pulse duration could be further compressed to ~200 fs by group-velocity-dispersion compensation outside the laser cavity, if needed, for future applications. The superior performance, massive production ability and environmental adaptability of the MoS_2-embedded fibre demonstrate its distinct advantages compared with a conventional 2D-materials-integrated fibre on the facets or external surfaces (Supplementary Tables 1 and 2), indicating that it is ready for scientific research and industrial applications in ultrafast lasers.

We predict that this two-step growth method can also be applied to grow other 2D materials (other than TMDs) onto optical fibres. For different applications, there are extremely rich choices of various 2D materials with different nonlinear properties. In addition, by fabricating well-designed fibre structures to control the group velocity dispersion, supercontinuum generation can be realized. Further, if phase matching between the excitation light and nonlinear signal is satisfied, the nonlinear conversion efficiency can even be increased to ~10% (Supplementary Fig. 14 and Supplementary Note 3), which would be comparable to that obtainable from conventional bulk optical crystals. If so, this can open a new regime for the design of nonlinear optical materials, which can inspire versatile nonlinear applications in optical fibres, such as sum-/difference-frequency generation, high-harmonic generation, nonlinear parametric amplification and terahertz sources.

Online content

Any methods, additional references, Nature Research reporting summaries, source data, extended data, supplementary information, acknowledgements, peer review information; details of author contributions and competing interests; and statements of data and code availability are available at https://doi.org/10.1038/s41565-020-0770-x.

Received: 22 April 2020; Accepted: 26 August 2020;
Published online: 21 September 2020

References

1. Cotter, D. et al. Nonlinear optics for high-speed digital information processing. *Science* **286**, 1523–1528 (1999).
2. Agrawal, G. P. Nonlinear fiber optics: its history and recent progress. *J. Opt. Soc. Am. B* **28**, A1–A10 (2011).
3. Granzow, N. et al. Supercontinuum generation in chalcogenide-silica step-index fibers. *Opt. Express* **19**, 21003–21010 (2011).
4. Markos, C. et al. Hybrid photonic-crystal fiber. *Rev. Mod. Phys.* **89**, 045003 (2017).
5. Sazio, P. J. et al. Microstructured optical fibers as high-pressure microfluidic reactors. *Science* **311**, 1583–1586 (2006).
6. Abouraddy, A. et al. Towards multimaterial multifunctional fibres that see, hear, sense and communicate. *Nat. Mater.* **6**, 336–347 (2007).
7. Eggleton, B. J., Luther-Davies, B. & Richardson, K. Chalcogenide photonics. *Nat. Photon.* **5**, 141–148 (2011).
8. Skryabin, D., Luan, F., Knight, J. & Russell, P. S. J. Soliton self-frequency shift cancellation in photonic crystal fibers. *Science* **301**, 1705–1708 (2003).
9. Dudley, J. M., Genty, G. & Coen, S. Supercontinuum generation in photonic crystal fiber. *Rev. Mod. Phys.* **78**, 1135–1184 (2006).
10. Dudley, J. M. & Taylor, J. R. Ten years of nonlinear optics in photonic crystal fibre. *Nat. Photon.* **3**, 85–90 (2009).
11. Autere, A. et al. Nonlinear optics with 2D layered materials. *Adv. Mater.* **30**, 1705963 (2018).
12. Li, Y. et al. Probing symmetry properties of few-layer MoS_2 and h-BN by optical second-harmonic generation. *Nano Lett.* **13**, 3329–3333 (2013).
13. Liu, X., Guo, Q. & Qiu, J. Emerging low-dimensional materials for nonlinear optics and ultrafast photonics. *Adv. Mater.* **29**, 1605886 (2017).
14. Liu, H. et al. High-harmonic generation from an atomically thin semiconductor. *Nat. Phys.* **13**, 262–265 (2017).
15. Wang, F. et al. Wideband-tuneable, nanotube mode-locked, fibre laser. *Nat. Nanotechnol.* **3**, 738–742 (2008).
16. Bao, Q. et al. Broadband graphene polarizer. *Nat. Photon.* **5**, 411–415 (2011).
17. Lee, E. J. et al. Active control of all-fibre graphene devices with electrical gating. *Nat. Commun.* **6**, 6851 (2015).
18. Chen, K. et al. Graphene photonic crystal fibre with strong and tunable light–matter interaction. *Nat. Photon.* **13**, 754–759 (2019).
19. Van Der Zande, A. M. et al. Grains and grain boundaries in highly crystalline monolayer molybdenum disulphide. *Nat. Mater.* **12**, 554–561 (2013).
20. Huang, C. et al. Lateral heterojunctions within monolayer $MoSe_2$–WSe_2 semiconductors. *Nat. Mater.* **13**, 1096–1101 (2014).
21. Li, M.-Y. et al. Epitaxial growth of a monolayer WSe_2-MoS_2 lateral p-n junction with an atomically sharp interface. *Science* **349**, 524–528 (2015).
22. Gao, Y. et al. Large-area synthesis of high-quality and uniform monolayer WS_2 on reusable Au foils. *Nat. Commun.* **6**, 8569 (2015).
23. Pistorius, C. W. Phase diagrams of sodium tungstate and sodium molybdate to 45 kbar. *J. Chem. Phys.* **44**, 4532–4537 (1966).
24. Yu, H. et al. Wafer-scale growth and transfer of highly-oriented monolayer MoS_2 continuous films. *ACS Nano* **11**, 12001–12007 (2017).
25. Lee, C. et al. Anomalous lattice vibrations of single- and few-layer MoS_2. *ACS Nano* **4**, 2695–2700 (2010).
26. Liu, K.-K. et al. Growth of large-area and highly crystalline MoS_2 thin layers on insulating substrates. *Nano Lett.* **12**, 1538–1544 (2012).
27. Shen, Y.-R. *The Principles of Nonlinear Optics* (Wiley, 1984).
28. Chen, J. H. et al. Tunable and enhanced light emission in hybrid WS_2-optical-fiber-nanowire structures. *Light Sci. Appl.* **8**, 8 (2019).
29. Jiang, B. et al. High-efficiency second-order nonlinear processes in an optical microfibre assisted by few-layer GaSe. *Light Sci. Appl.* **9**, 63 (2020).
30. Zhang, H. et al. Molybdenum disulfide (MoS_2) as a broadband saturable absorber for ultra-fast photonics. *Opt. Express* **22**, 7249–7260 (2014).

Methods

Pre-deposition of transition metal feedstock into optical fibres. Transition metal sources (Mo or W) were pre-deposited on the fibres by capillarity of their corresponding saline solutions at optimized concentrations. For monolayer film growth, the amount of metal precursor was tuned according to the hole diameters of the different fibres. Typical concentrations are as follows: Na_2MoO_4 at 8, 21 and 45 mg ml^{-1} or Na_2WO_4 at 12, 30 and 64 mg ml^{-1} for HCF with core diameters of 50, 15 and 5 μm, respectively; Na_2MoO_4 at 32 and 54 mg ml^{-1} or Na_2WO_4 at 45 and 72 mg ml^{-1} for PCF with hollow- and solid-core honeycomb structures, respectively. Then, the fibres were heated to 110 °C and dried in an argon atmosphere for 30 min before CVD growth.

Syntheses of TMD-embedded optical fibres. The Mo-precursor-based pre-deposited fibres were placed on a quartz plate in the centre of the CVD furnace, and 1 g sulfur (99%, Sigma Aldrich) powder was placed in the upstream region outside the heating zone. Then, the chamber of the furnace was flushed with argon for creating an inert atmosphere and subsequently ramped up to the optimized growth temperature (~820 °C for MoS_2 growth) with 100 s.c.c.m. argon. During the growth, the temperature for sulfur evaporation was ~120 °C. The entire process was carried out under ~150 Pa, and the growth duration was set as 15–30 min. After the growth, the system was naturally cooled down to room temperature. Similar growth conditions were used to synthesize other TMD and alloy fibres, such as $MoSe_2$, WS_2 and MoS_xSe_{2-x}, except for different temperatures for chalcogen sublimation and TMD growth. In particular, the sublimation temperatures were ~120 °C for sulfur and ~220 °C for selenium, and the growth temperatures were ~800, ~950 and ~820 °C for $MoSe_2$-, WS_2- and MoS_xSe_{2-x}-embedded fibres, respectively.

Characterization of TMD-embedded optical fibres. Optical images were taken with an Olympus BX51M microscope by focusing on the holes of the fibre walls. Raman and PL spectra were collected with a homemade optical system excited using a 532 nm laser with power of ~1 mW. STEM (FEI Titan Themis G2 300) was conducted to characterize the atomic structure, and a scanning electron microscope (Thermo Fisher, Quattro S) was used to characterize the morphology of the samples.

Harmonic generation measurements. An optical parameter oscillator (Coherent, Mira-OPO-X) pumped by a titanium–sapphire oscillator (Coherent, Mira-HP) provided a wavelength-tunable excitation laser (15 mW, ~150 fs, 76 MHz) and then it was focused onto the MoS_2 HCF or MoS_2/silica via an objective (Nikon, ×10, NA = 0.25). The SHG and THG signals were collected by a spectrograph with a silicon-based charge-coupled device (Princeton Instruments, SP2500 and PyLoN 400BRX) via a transmission system.

Saturable absorption measurements. A homemade pulsed fibre laser (200 fs, 1,564 nm, 75.4 MHz) was utilized to measure the power-dependence transmission of MoS_2 PCF. The pulsed laser was equally divided using a fibre-optic coupler to monitor the power. The input/output single-mode fibre (Corning, SMF-28e+) was aligned with a 3-cm-long MoS_2 PCF (NKT Photonics, HC-1550) by a homemade alignment setup that included two optical microscopes along different directions and multi-axis stages to ensure accurate alignment.

Implementation and characterization of all-fibre mode-locked laser. A laser diode (600 mW, 976 nm) was coupled into the fibre ring cavity via a wavelength-division multiplexer as the pump source and 60-cm-long erbium-doped fibre (LIEKKI, Er110) as the gain medium. An isolator guaranteed that the laser in the fibre ring was transferred along a single direction. In this case, we employed a backward pumping configuration for large output power. Further, 3-cm-long MoS_2 PCF was integrated as the SA with a coupler for 20% output. An additional polarization controller was utilized to optimize the output spectrum and pulse width. The total group velocity dispersion of the fibre ring was 0.0005 ps^2, comprising a 1 m single-mode fibre, 0.6 m erbium-doped fibre and 3.4 m OSF980 (as the dispersion compensation fibre) with group velocity dispersion of −22, +12 and +4.5 fs^2 mm^{-1}, respectively. The output spectra and autocorrelation trace were measured by a spectrograph with an infrared charge-coupled device (Princeton Instruments; HRS-300SS with a grating of 150 grooves mm^{-1} and NIRvana 640 with spectrometer resolution of ~1.3 nm) and an autocorrelator (APE, pulseCheck USB-15). The pulse train and signal-to-noise ratio were observed by an oscilloscope (Rigol, DS6104) and radio-frequency spectrograph (Rigol, DSA815). A self-starting mode-locked pulse was observed when the pump power was increased to 180 mW.

Reporting Summary. Further information on research design is available in the Nature Research Reporting Summary linked to this article.

Data availability

The authors declare that the data supporting the findings of this study are available within the paper, Supplementary Information and Source Data. Extra data are available from the corresponding authors upon request. Source data are provided with this paper.

Acknowledgements

This work was supported by the National Natural Science Foundation of China (51991340, 51991342, 51991344 and 51421002); National Key R&D Program of China (2016YFA0300903 and 2016YFA0300804); Beijing Natural Science Foundation (JQ19004); Beijing Excellent Talents Training Support (2017000026833ZK11); Beijing Graphene Innovation Program (Z181100004818003); Beijing Municipal Science & Technology Commission (Z191100007219005); the Key R&D Program of Guangdong Province (2019B010931001, 2020B010189001, 2018B010109009 and 2018B030327001); Guangdong Innovative and Entrepreneurial Research Team Program (2016ZT06D348); Bureau of Industry and Information Technology of Shenzhen (graphene platform 201901161512); the Science, Technology and Innovation Commission of Shenzhen Municipality (KYTDPT20181011104202253); Program of Chinese Academy of Sciences (ZDYZ2015-1 and XDB33030200); National Postdoctoral Program for Innovative Talents (BX20180013 and BX20190016); the Academy of Finland; the ERC (834742); the European Union's Horizon 2020 research and innovation programme (820423, S2QUIP); and China Postdoctoral Science Foundation (2019M660001, 2019M660280 and 2019M660281). We acknowledge the Electron Microscopy Laboratory in Peking University for the use of their electron microscope.

Author contributions

Z.L., X.B. and K.L. conceived the experiments and supervised the project. Y.G.Z. and C.L. contributed to the growth experiments. W.Y. performed the optical experiments and fibre laser setup. X.C. contributed to the theoretical modelling. R.Q., P.G. and X.B. conducted the STEM experiments. J.L., X.Z., J.W., M.W. and Y.Z. conducted the SEM, PL and Raman characterizations. S.W. and Z.S. suggested the optical experiments. All the authors discussed the results and wrote the manuscript.

Competing interests

The authors declare no competing interests.

Additional information

Supplementary information is available for this paper at https://doi.org/10.1038/s41565-020-0770-x.

Correspondence and requests for materials should be addressed to K.L., X.B. or Z.L.

Peer review information *Nature Nanotechnology* thanks Baohua Jia, Zhiyi Wei and the other, anonymous, reviewer(s) for their contribution to the peer review of this work.